



## OPEN ACCESS

## EDITED BY

Maria Ines Gimenez,  
National University of Mar del Plata, Argentina

## REVIEWED BY

Tushar Kant Beuria,  
Institute of Life Sciences (ILS), India  
Yaodong Chen,  
Northwest University, China

## \*CORRESPONDENCE

Sonja-Verena Albers  
[sonja.albers@biologie.uni-freiburg.de](mailto:sonja.albers@biologie.uni-freiburg.de)

## 'PRESENT ADDRESSES

Megha Patro,  
Structural and Computational Biology Unit,  
European Molecular Biology Laboratory,  
Heidelberg, Germany  
Solenne Ithurbide,  
Département de Microbiologie, Infectiologie  
et Immunologie, Université de Montréal,  
Montréal, QC, Canada

RECEIVED 01 August 2024

ACCEPTED 02 October 2024

PUBLISHED 12 November 2024

## CITATION

Patro M, Grünberger F, Sivabalasarma S, Gfrerer S, Rodriguez-Franco M, Nußbaum P, Grohmann D, Ithurbide S and Albers S-V (2024) Mind2 modulates cell shape and motility in the archaeon *Haloferax volcanii*. *Front. Microbiol.* 15:1474570.  
doi: 10.3389/fmicb.2024.1474570

## COPYRIGHT

© 2024 Patro, Grünberger, Sivabalasarma, Gfrerer, Rodriguez-Franco, Nußbaum, Grohmann, Ithurbide and Albers. This is an open-access article distributed under the terms of the [Creative Commons Attribution License \(CC BY\)](#). The use, distribution or reproduction in other forums is permitted, provided the original author(s) and the copyright owner(s) are credited and that the original publication in this journal is cited, in accordance with accepted academic practice. No use, distribution or reproduction is permitted which does not comply with these terms.

# MinD2 modulates cell shape and motility in the archaeon *Haloferax volcanii*

Megha Patro<sup>1,2†</sup>, Felix Grünberger<sup>3</sup>, Shamphavi Sivabalasarma<sup>1,2</sup>, Sabrina Gfrerer<sup>1</sup>, Marta Rodriguez-Franco<sup>4</sup>, Phillip Nußbaum<sup>1</sup>, Dina Grohmann<sup>3</sup>, Solenne Ithurbide<sup>1†</sup> and Sonja-Verena Albers<sup>1,\*</sup>

<sup>1</sup>Molecular Biology of Archaea, Institute of Biology, Faculty of Biology, University of Freiburg, Freiburg, Germany, <sup>2</sup>Spemann Graduate School of Biology and Medicine, University of Freiburg, Freiburg, Germany, <sup>3</sup>Institute of Biochemistry Genetics and Microbiology, Institute of Microbiology and Archaea Centre, Single-Molecule Biochemistry Lab & Biochemistry Centre Regensburg, University of Regensburg, Regensburg, Germany, <sup>4</sup>Cell Biology, Institute of Biology, Faculty of Biology, University of Freiburg, Freiburg, Germany, <sup>5</sup>Signalling Research Centres BIOSS and CIBSS, University of Freiburg, Freiburg, Germany

In bacteria and archaea, proteins of the ParA/MinD family of ATPases regulate the spatiotemporal organization of various cellular cargoes, including cell division proteins, motility structures, chemotaxis systems, and chromosomes. In bacteria, such as *Escherichia coli*, MinD proteins are crucial for the correct placement of the Z-ring at mid-cell during cell division. However, previous studies have shown that none of the 4 MinD homologs present in the archaeon *Haloferax volcanii* have a role in cell division, suggesting that these proteins regulate different cellular processes in haloarchaea. Here, we show that while deletion of MinD2 in *H. volcanii* ( $\Delta minD2$ ) does not affect cell growth or division, it impacts cell shape and motility by mispositioning the chemotaxis arrays and archaellum motors. Finally, we explore the links between MinD2 and MinD4, which has been previously shown to modulate the localization of chemosensory arrays and archaella in *H. volcanii*, finding that the two MinD homologues have synergistic effects in regulating the positioning of the motility machinery. Collectively, our findings identify MinD2 as an important link between cell shape and motility in *H. volcanii* and further our understanding of the mechanisms by which multiple MinD proteins regulate cellular functions in haloarchaea.

## KEYWORDS

*Haloferax volcanii*, archaea, cell shape, shape transition, light and fluorescence microscopy, protein localisation, motility

## Introduction

A proper spatial distribution of cellular components is essential for the optimal functioning of cells. In bacteria and archaea, the ParA/MinD family of ATPases is crucial for the spatiotemporal organization of various cellular cargoes. For example, ParA proteins are involved in plasmid partitioning and chromosome segregation (Baxter and Funnell, 2014; Jalal and Le, 2020), while MinD is known for its role in regulating the placement of the bacterial divisome (Lutkenhaus, 2007). However, ParA/MinD proteins are not restricted to these functions and have been shown to modulate the positioning of several other cellular components, including flagella (Pulianmackal et al., 2023; Pradhan et al., 2024), chemotaxis systems (Ringgaard et al., 2011), and the conjugation machinery (Atmakuri et al., 2007).

Although several ParA/MinD homologs are encoded in archaeal genomes, their distribution and functions are still being elucidated. Notably, while ParA can be found in almost all archaea, only Euryarchaeota encode for MinD homologs (Nußbaum et al., 2020). Furthermore, although a few structural analyses have been carried on archaeal MinD homologs (*Pyrococcus horikoshii*, *Pyrococcus furiosus* and *Archaeoglobus fulgidus*) (Jeoung et al., 2009; Szklarczyk et al., 2017), the functional roles of MinD have so far only been studied in *H. volcanii* (Nußbaum et al., 2020). *H. volcanii* encodes for 4 MinD homologs: *minD1* (HVO\_0225), *minD2* (HVO\_0595), *minD3* (HVO\_1634) and *minD4* (HVO\_0322). Notably, in contrast to the critical role of MinDs in regulating cell division in bacteria, deletion of all 4 MinD homologs had no role in cell division or growth in *H. volcanii* (Nußbaum et al., 2020). However, deletion of MinD4 reduced archaeal swimming motility due to the mispositioning of chemotaxis arrays and archaellum motors, suggesting a significant role of MinD4 in governing these processes (Nußbaum et al., 2020). However, the role of other MinD homologues remains unclear.

In this study, we characterized the functions of the MinD2 protein of *H. volcanii*. Since MinD2 was observed to not directly affect FtsZ localization (and thus cell division) or cell growth, it suggests a role in other cellular pathways (Nußbaum et al., 2020). Using genetic mutants, we showed it has a crucial role in determining cell shape, influencing the transition from rod-shaped to plate-shaped cells. Furthermore, using fluorescently tagged MinD2 variants, we demonstrated that the protein has a diffused localization pattern, which suggests a potential regulatory mechanism for its cellular functions, possibly involving interactions with partner proteins. Additionally, we demonstrated that MinD2 synergizes with MinD4 to modulate chemosensory array localization, archaella assembly and motility, further illustrating the role of MinD2 homologues in spatial organization. Overall, our findings contribute to a deeper understanding of the function of MinD2 in *H. volcanii*, highlighting its multifaceted role in coordinating cellular morphology and motility.

## Results

### MinD2 impacts cell shape

To elucidate the function of MinD2 in *H. volcanii*, we started by characterizing the growth of a mutant strain lacking MinD2 ( $\Delta minD2$ ). Growth rate measurements showed that the  $\Delta minD2$  strain exhibited a growth pattern similar to that of the wild-type (WT) strain H26 (Supplementary Figure 1), suggesting that MinD2 does not directly influence growth in *H. volcanii* as previously shown by Nußbaum et al. (2020).

Then, we assessed the impact of MinD2 on morphology, using phase contrast microscopy to compare the cell shape and size of WT vs.  $\Delta minD2$  cells during different growth stages. As previously described, we found that WT *H. volcanii* (H26) undergoes growth-dependent alterations in its cell morphology. The time point of this shape transition has been observed to differ greatly based on medium components and is also affected by the presence of plasmids (Li et al., 2019; de Silva et al., 2021; Patro et al., 2023). During the early log phase, the liquid culture is predominantly composed of rod-shaped cells (R), which gradually transition into an intermediate state (I) and then into plate-shaped cells (P) as the optical density ( $OD_{600}$ ) of the

culture increases. The categorization of cell shape was conducted as previously described in Patro et al. (2023). Indeed, H26 (WT) cells predominantly exhibited rod-shaped morphology until an  $OD_{600}$  of 0.03, with a minority showing I or P shapes ( $R = 41\%$ ;  $I = 26\%$ ;  $P = 33\%$ ) (Figure 1 and Supplementary Figure 2a). Starting from an  $OD_{600}$  of 0.06, a noticeable transition towards P cells became evident, with plates representing the majority ( $P = 55\%$ ). This trend persisted as the culture progressed, with the frequency of P cells reaching 81% at an  $OD_{600}$  of 0.2. By contrast, the majority of  $\Delta minD2$  cells exhibited a plate-shaped morphology even in the early log phase ( $OD_{600} 0.01$ ), with few I and R cells ( $R = 17\%$ ;  $I = 33\%$ ;  $P = 50\%$ ) (Figure 1 and Supplementary Figure 2a). The frequency of P cells continued to increase at higher culture densities, with more than 80% of the cell population adopting a plate-shaped morphology at  $OD_{600}$  above 0.06 (Figure 1 and Supplementary Figure 1).

Additionally, a comparison of the cell area in both strains displayed a similar trend, with  $\Delta minD2$  cells having significantly smaller areas than WT cells at an  $OD_{600}$  of 0.01 (Supplementary Figure 2b). Nevertheless, the areas of both WT and  $\Delta minD2$  cells were comparable at higher densities ( $OD_{600} \geq 0.03$ ).

Collectively, these analyses demonstrate that while MinD2 does not affect cell growth, it significantly influences cell shape, with the deletion of *minD2* resulting in the loss of the ability to maintain a rod-shaped morphology, particularly in the early growth phase.

Previously, we found that the presence of a plasmid played a transient role in maintaining rod-shaped morphology in *H. volcanii* (Patro et al., 2023). To test this, we looked at the effects of deleting the MinD2 gene on cell shape and size, with or without the empty plasmid pTA1392. In the WT (H26) cells, when the plasmid was present, the cells changed from rods to plates between  $OD_{600} 0.06$  and 0.1. Without the plasmid, this switch happened earlier, between  $OD_{600} 0.03$  and 0.06 (Supplementary Figure 1b; Patro et al., 2023). Similarly, in MinD2 mutants, more cells were rod-shaped at  $OD_{600} 0.01$  when pTA1392 was present. Without the plasmid, these mutant cells were mostly plate-shaped at  $OD_{600} 0.01$ . In MinD2 mutants with pTA1392, cells shifted to an intermediate shape (39%) at  $OD_{600} 0.03$  and mostly plate-shaped (40%) at  $OD_{600} 0.06$ . This shape change happened one generation earlier in the MinD2 mutants with pTA1392 compared to WT cells with the plasmid. These results highlight MinD2's role in modulating cell shape, especially in becoming plate-shaped. The plasmid increases the number of rod-shaped cells in the MinD2 mutant, promoting rod development. Furthermore, while cells that contained plasmids maintained rod-shaped morphology longer throughout the different growth phases, the absence of *minD2* still reduced the ability to maintain a rod-shaped morphology throughout all phases (Supplementary Figures 1b, 2c,d).

### MinD2 deletion impacts the assembly of archaella

In *H. volcanii*, cell shape is linked to swimming motility. During the early logarithmic phase, rod-shaped *H. volcanii* cells exhibit motility, powered by the assembly of polar bundles of archaella (Li et al., 2019). However, as cells transition into plate shape during stationary phase, the archaellum filaments are lost, resulting in motility cessation. Given the observed impact of MinD2 deletion on cell shape, we investigated whether the  $\Delta minD2$  also showed changes

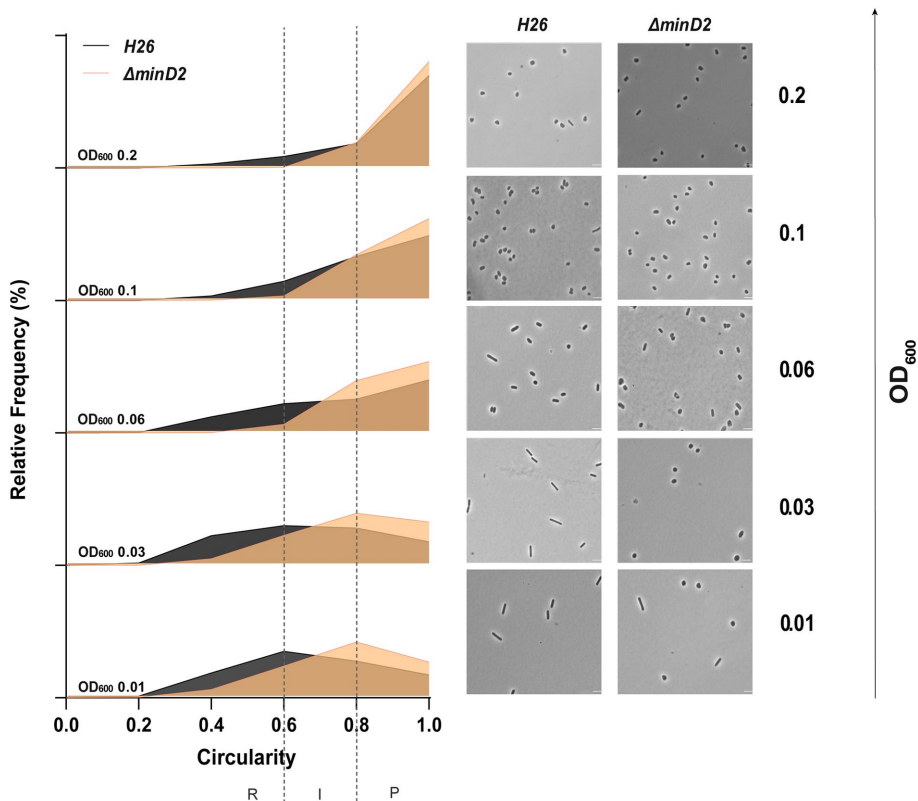


FIGURE 1

Cell shape analysis in  $\Delta minD2$  strain and wild-type H26 cells throughout the growth curve. Left: Relative frequency distribution of cell circularity comparing H26 (grey) and  $\Delta minD2$  (orange) analyzed from micrographs. Vertical dashed line represents the different cell type R, rods; I, intermediates and P, Plates. Sum of the graph height per OD<sub>600</sub> equals 100% and Y-axis indicates the percentage of cell population per cell type. Right: Phase contrast micrographs showing H26 and  $\Delta minD2$  at different growth stages from OD<sub>600</sub> 0.01 to 0.2 (bottom to top). Scale bar: 4  $\mu$ m.  $n_{H26} > 1745$ ,  $n_{\Delta minD2} > 1,535$ . Three independent experiments with biological triplicates were carried out for both the strains.

in archaella assembly and motility. For this, we used transmission electron microscopy (TEM) to characterize WT and  $\Delta minD2$  cells collected at an early log phase (OD<sub>600</sub> 0.03). However, *H. volcanii* cells express several pili throughout different growth phases (Esquivel et al., 2016), which are difficult to differentiate in diameter and size from archaella. Therefore, we further deleted *pilB3*, the pilus assembly ATPase, in both the H26 and  $\Delta minD2$  strain. These  $\Delta pilB3$  mutants lack pili, which facilitates visualization of archaella in these strains.

The results revealed that the rod-shaped H26 $\Delta pilB3$  cells, both with and without plasmid pTA1392, displayed archaellation in 80 and 83.7% of the cells, respectively (Figures 2a,c). By contrast, the  $\Delta minD2\Delta pilB3$  strain, characterized by a discoid-shaped phenotype, only the few rod-shaped cells observed showed archaellation (~20% of the cells). In the presence of pTA1392, where the percentage of rod-shaped cells is slightly increased (24%; Supplementary Figures 2a,b), the percentage of archaellated cells is also observed to increase to ~32% (Figures 2b,c).

Given the observed effects of MinD2 deletion on archaellation levels, we investigated whether this impacted the motility of the  $\Delta minD2$  strain, by growing the cells on soft agar plates. First, we found that  $\Delta minD2$  strain grown in nutrient-rich YPC media showed reduced motility compared to H26 (data not shown). However, due to the composition of the medium, cell growth was rapid, making it difficult to differentiate growth from swimming halos in soft agar plates. Therefore, we switched to a different medium (CA), where

strains grow slower. In order to support growth on CA medium, which lacks uracil, strains were transformed with a plasmid (pTA1392) containing the *pyrE2* locus (which enables uracil biosynthesis). Using this strategy, we observed that  $\Delta minD2$  + pTA1392 cells exhibited a swimming defect, with their motility being only ~25% of what was observed for H26 + pTA1392 cells (Figure 2d). We were able to complement the  $\Delta minD2$  motility defect by expression of MinD2 on plasmid pTA1392 (pSVA6011, Figure 3). Additionally, the observed reduction in motility in  $\Delta minD2$  was consistent with the lower number of mutant cells assembling archaella.

The hallmark of ParA/MinD superfamily proteins is the Walker A (WA) and Walker B (WB) motif (Leipe et al., 2002; Hu and Lutkenhaus, 2003). Mutation of both the motif in MinD4 had previously displayed motility phenotype and disrupted MinD4's localization at poles (Nußbaum et al., 2020). We wanted to investigate the role of the WA and WB motifs of MinD2 by generating plasmids with WA (K16A) mutant and WB (D117A). Expressing these in  $\Delta minD2$  strain, we observed that mutation of WA did not have an effect on the swimming motility, and the strain had 100% activity as visualized in the wild type (H26). Whereas the WB mutant showed a defect in motility (~30%) similar to  $\Delta minD2$  deletion mutant strain (Supplementary Figure 4).

Thus, these results confirm that MinD2 not only modulates cell shape but also impacts cell motility, and that Walker B motif of MinD2 plays a role in the motility phenotype.

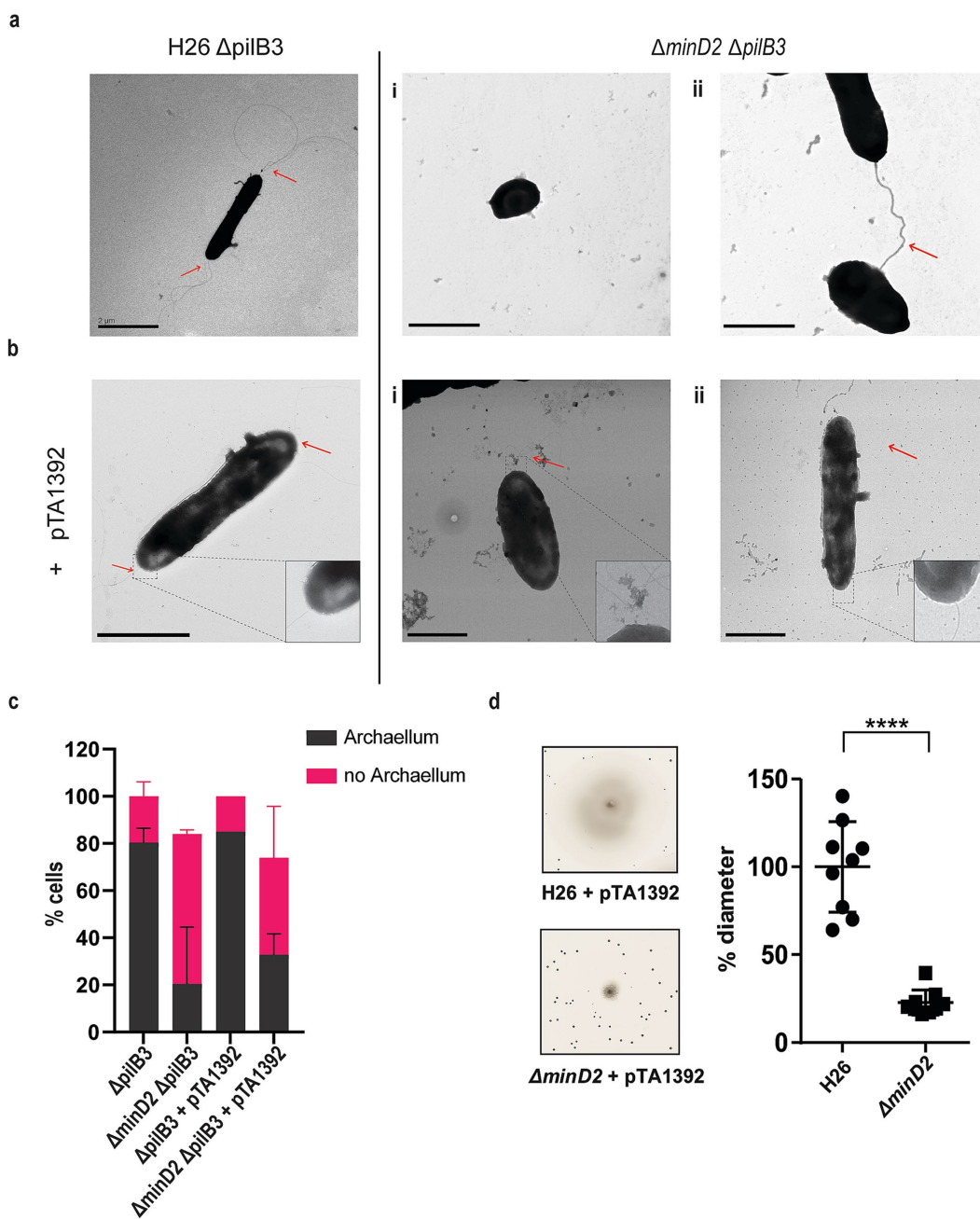


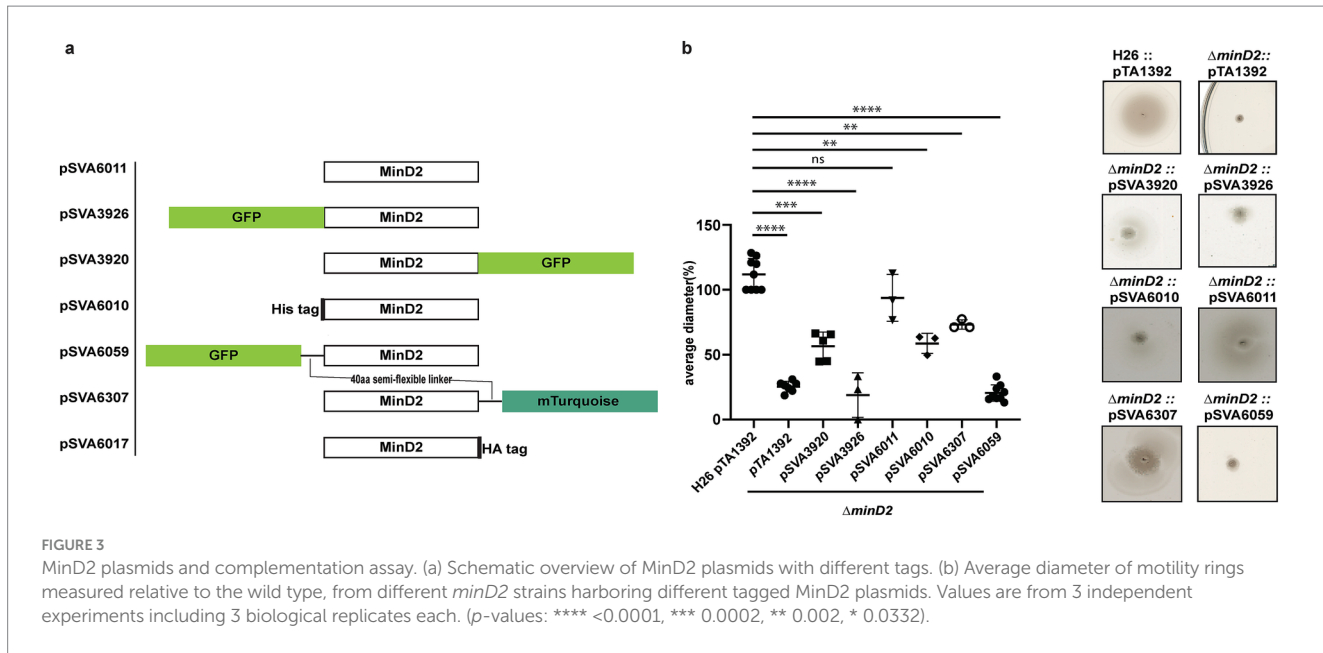
FIGURE 2

The deletion of *minD2* affects cell motility and archaellation. (a) Transmission electron microscopy of *H26 ΔpilB3* cells showing archaella and *ΔpilB3ΔminD2* (i) plate-shaped cell without archaella and (ii) rod shaped cell with archaella. (b) *H26 ΔpilB3 + pTA1392* cells showing archaella and *ΔpilB3ΔminD2 + pTA1392* (i) cell in transition rod to round (ii) rod shaped cell showing archaella. All cells were visualized at an early exponential phase ( $OD_{600}$ : 0.03). Scale bar: 2 μm. (c) Distribution of cells with or without archaella for *H26 ΔpilB3* and *ΔminD2* in the presence and absence of plasmid *pTA1392* from TEM analyzed cells.  $n_{\Delta p i l B 3} = 51$ ,  $n_{\Delta m i n D 2} = 54$ ,  $n_{\Delta p i l B 3 + p T A 1392} = 51$ ,  $n_{\Delta m i n D 2 + p T A 1392} = 40$  and  $n_{\Delta m i n D 2 + p T A 1392} = 59$ . (d) Semi-solid agar-based motility assay to visualize the swimming ability of *H26* and *ΔminD2*. Left panel: representative inserts; right panel: average diameter of the motility rings. Graph represents values from 3 technical replicates from 3 different biological replicates. \*\*\*\*  $p < 0.0001$ . Red arrow indicates the archaellum.

## Fluorescently tagged MinD2 shows diffused localization

The observed impact of MinD2 on motility is reminiscent of the role of MinD4, which we previously showed to be a MinD homologue that oscillates along the cell axis in *H. volcanii* and stimulates the formation of chemosensory arrays and archaella at

the cell poles, thereby regulating motility (Nußbaum et al., 2020). Therefore, we proceeded to examine the localization pattern of MinD2, by generating fluorescent fusion proteins. For this, the MinD2 protein was tagged at the N-or C-terminus with various tags and linkers, which were then expressed in the *ΔminD2* deletion mutant. To test whether the fluorescent tag had an impact on the function of MinD2, we performed complementation experiments



and assessed their motility using motility assays (Figure 3b). Notably, when a tag-less MinD2 variant was used (pSVA6011), the swimming phenotype could be restored to ~91% of the activity observed in WT cells. Expression of an N-terminal His-tag MinD2 variant (pSVA6010) restored ~62% of the motility activity, whereas the strain expressing an N-terminally tagged GFP variant (pSVA3926) had a motility defect similar to the  $\Delta\text{minD2}$  strain (Figure 3b) and showed diffuse localization in the cells (Supplementary Figure 3). Expression of a variant in which MinD2 was fused to an N-terminal GFP tag with a semi-flexible linker (Ithurbide et al., 2024) (pSVA6059) could also not restore motility. Tagging MinD2 on the C-terminus was, in general, more effective at restoring motility. Using only an HA tag at the C-terminus complemented the swimming back to 100% (Supplementary Figure 4). And, the strain expressing a C-terminally GFP tagged MinD2 variant (pSVA3920) retained ~60% of the motility displayed by WT cells, and the introduction of a semi-flexible linker between MinD2 and a C-terminal mTurquoise tag (pSVA6307) led to a restored swimming efficiency up to ~80% of that observed in H26 cells (Figure 3 and Supplementary Table 4).

We then proceeded to characterize the localization of the most functional C-term fluorescently tagged MinD2 variants. For this, samples were collected at similar OD<sub>600</sub>s as that of the cell shape experiments. Visualization of both the C-terminally GFP tagged and C-terminally mTurquoise tagged MinD2 variants showed a diffused localization throughout the cells (Supplementary Figure 3b) and from early log phase through mid-log phase. Based on our observations, MinD2-linker-mturquoise did not show a change in localization during the transition from rod to plate phases and does not show a different localization in rods versus in plates. Collectively, these data show that MinD2 does not localize to the cell poles, suggesting that its impact on the polar organization of the motility machinery likely requires the interaction of MinD2 with other proteins. Furthermore, the inability of N-terminally tagged MinD2 to complement the swimming phenotype suggests that the N-terminus of MinD2 is important for its activity and interaction with protein partners *in vivo*.

## Possible interaction partners of MinD2

### HVO\_0596

HVO\_0596 is a protein of unknown function encoded downstream of the *minD2* gene, likely within the same operon (Babski et al., 2016; Figure 4a). Synteny report on MinD2 and HVO\_0596 shows the two gene to be conserved in Haloarchaea (Supplementary Table 5). Furthermore, an AlphaFold 3 (Abramson et al., 2024) prediction indicated a possible interaction between MinD2 and HVO\_0596, based on 6 hydrogen bonds between 5 residues of HVO\_0596 at the C-terminus and the C-terminus of MinD2 with an iPTM score = 0.83 and pTM = 0.63 (Figure 4b). To explore a potential role of HVO\_0596 in MinD2 functionality, we generated a deletion mutant for HVO\_0596 and a double deletion mutant  $\Delta\text{hvo\_0596}\Delta\text{minD2}$ . The  $\Delta\text{hvo\_0596}$  deletion mutant showed no discernible impairment of cell growth (Figure 4c) and to the contrary of *minD2* deletion, *the deletion of HVO\_0596 has no effect on cell shape development and transition during growth* (Figure 4d).

Additionally, no soft-agar motility defect could be observed for the single mutant  $\Delta\text{hvo\_0596}$  and the double deletion mutant  $\Delta\text{hvo\_0596}\Delta\text{minD2}$  exhibited the same motility defect as the  $\Delta\text{minD2}$  deletion mutant (Figure 4e). These results suggest that HVO\_0596 does not directly affect motility.

To elucidate the localization pattern of HVO\_0596, we generated a fluorescently tagged version of HVO\_0596 at its N-terminus with mNeongreen (pSVA6051). Localization experiments showed diffuse fluorescence in both deletion mutants  $\Delta\text{hvo\_0596}$ ,  $\Delta\text{minD2}$  and  $\Delta\text{hvo\_0596}\Delta\text{minD2}$  (Figure 4f).

### CetZ5 and CetZ6

*Haloferax volcanii* has 6 paralogues of CetZs of which CetZ1 and CetZ2 have been studied for their role as cytoskeletal proteins and role in motility (Brown et al., 2024). An accompanying study by Brown et al. (2024, unpublished) suggests a possible interaction between MinD2 and CetZ1. Specifically, MinD2 was found to influence the cellular positioning of CetZ1, impacting its polar localization. While

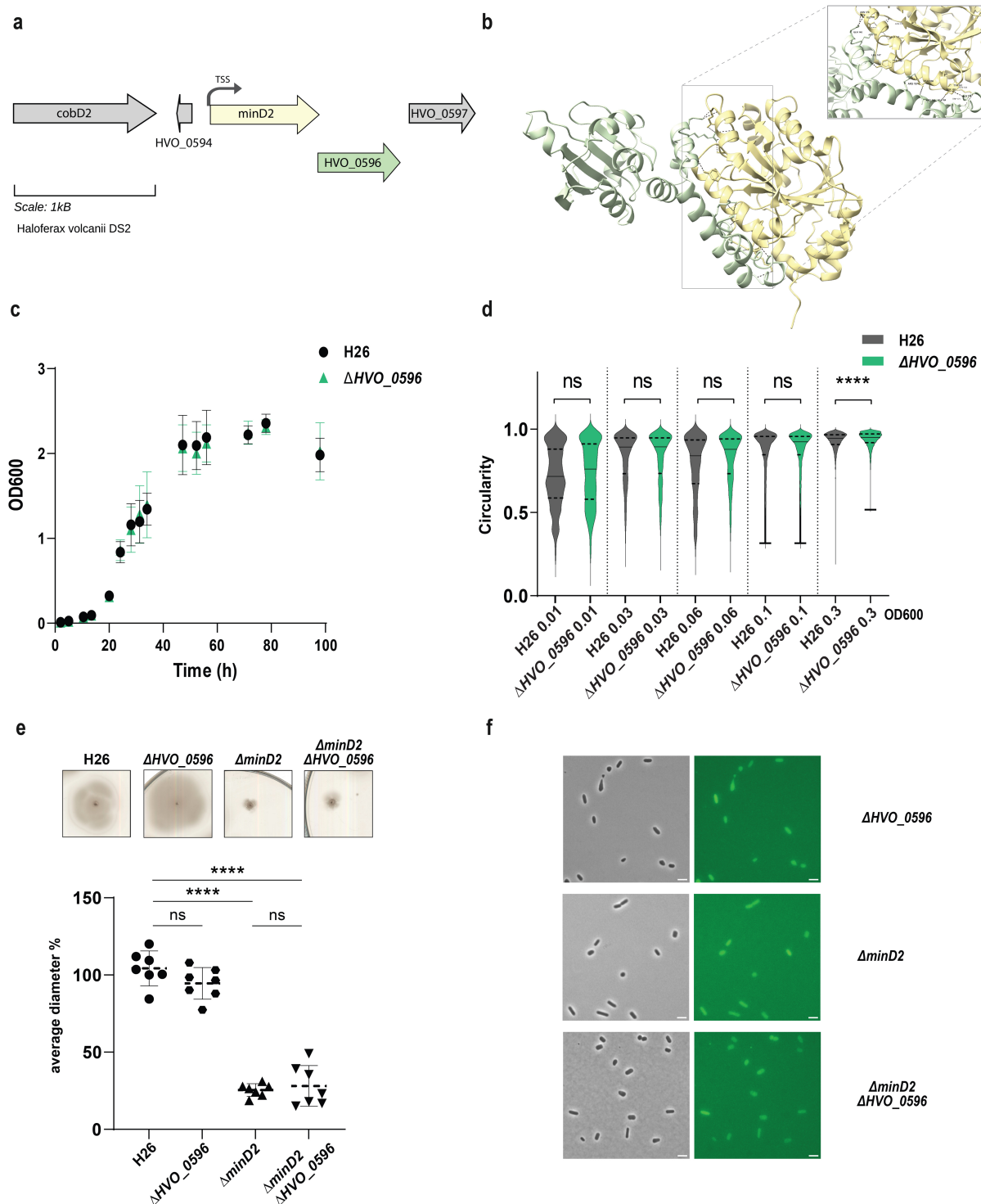


FIGURE 4

*HVO\_0596* might interact with *MinD2* but its deletion mutant has no phenotypes. (a) Schematic representation of the gene neighborhood showing *MinD2* (*HVO\_0595*) (yellow) and *HVO\_0596* (green) showing the TSS (black arrow) present 28 bp upstream of start. (b) Alphafold 3 prediction revealing interaction between *MinD2* and *HVO\_0596*. Black dashed lines indicates the intermolecular H-bond at the C-terminus of both proteins and red dashed line indicates the interaction found with relaxed angle criteria in ChimeraX. (c) Growth curve of H26 (black) and  $\Delta HVO_0596$  (green). (d) Distribution of cell circularity (%) at different ODs;  $n > 1100$ . (e) Quantification (bottom panel) of motility diameter for by the different mutants and WT (inserts: Top Panel). Calculations were made using 3 independent experiments including  $>2$  biological replicates each. Black line indicates mean, lower, and upper lines the standard deviation. (f) Representative inserts of mNeonGreen-*HVO\_0596* localization in H26(WT) and deletion mutants  $\Delta HVO_0596$ ,  $\Delta minD2$  and  $\Delta HVO_0596 minD2$ . Scale bar: 4  $\mu$ m.

the function of the other four CetZs is uncharacterized, CetZ5 was hypothesized to be a cytoskeletal protein by Schiller et al. (2024). It is therefore possible that MinD2 interacts with these CetZ proteins in the cell. Therefore, we wanted to address possible interactions with CetZ5 and CetZ6.

CetZ5 and CetZ6, initially characterized as FtsZ7 and FtsZ8, belong to the tubulin/FtsZ family, and previous studies have shown that deleting these proteins has no effect on cell division (Duggin et al., 2015). To characterize the role of these proteins with respect to MinD2, we generated single deletion mutants ( $\Delta$ cetZ5 and  $\Delta$ cetZ6) and double deletion mutants with minD2 ( $\Delta$ cetZ5 $\Delta$ minD2 and  $\Delta$ cetZ6 $\Delta$ minD2). We found no motility defects for either  $\Delta$ cetZ5 or  $\Delta$ cetZ6 (Figures 5a,c) as observed previously (Duggin et al., 2015). The double deletion mutants ( $\Delta$ cetZ5 $\Delta$ minD2 and  $\Delta$ cetZ6 $\Delta$ minD2) showed reduced motility similar to that of the single  $\Delta$ minD2 mutant, indicating that the impact in swimming ability is due to deletion of MinD2 rather than these CetZ proteins.

To gain insight into the cellular positioning of the CetZ proteins, we created N-terminally GFP tagged versions of CetZ5 (pSVA6040) and CetZ6 (pSVA6042). In both cases, the localization of the proteins was diffused across the cells (Figures 5c,d). To check if cell shape has an effect on CetZ localization, we further visualized the distribution of the tagged proteins at different ODs. However, both GFP-CetZ5 and GFP-CetZ6 displayed diffused fluorescence throughout all the growth phases analyzed (Figures 5c,d).

Collectively, our experiments indicate no direct interaction of HVO\_0596, CetZ5, and CetZ6 with MinD2.

## MinD2 regulates the positioning of the motility and chemotactic machineries

Given that the  $\Delta$ minD2 mutant exhibited a motility defect and displayed reduced assembly of archaella, we hypothesized that MinD2 may have a function similar to that of MinD4 with respect to the cellular positioning of the motility and chemotactic machineries. Therefore, we investigated the localization of the motility machinery in  $\Delta$ minD2. For this, we used strains expressing ArlD-GFP, a fluorescently tagged version of a well-established marker protein, which is part of the cytoplasmic archaellum motor complex, used as an indicator to identify cells with archaella (Li et al., 2019). Upon expression of ArlD-GFP in the  $\Delta$ arlD strain at OD<sub>600</sub> 0.01, we observed that most cells (77%) had fluorescent foci at the cell poles, with only a few cells displaying diffused fluorescence (23%) (Figures 6a,b), similar to results previously observed in *H. volcanii* (Li et al., 2019). However, when ArlD-GFP was expressed in  $\Delta$ minD2 $\Delta$ arlD cells, fluorescent foci at the poles were only detected in 25% of the cells (Figures 6a,b). This result agrees with the low abundance of archaella observed in TEM, where these structures were present in only ~32% of  $\Delta$ minD2 $\Delta$ pilB3 (+ pTA1392) cells (Figure 2).

As described above, in previous studies we established a correlation between MinD4 and the positioning of the archaellum machinery. Therefore, we decided to explore the links between MinD2 and MinD4 in the regulation of this process, by comparing the localization of the motility machinery in cells lacking either one of the MinD homologues ( $\Delta$ minD2 $\Delta$ arlD or  $\Delta$ minD4 $\Delta$ arlD) or both homologues ( $\Delta$ minD2 $\Delta$ minD4 $\Delta$ arlD). In the  $\Delta$ minD4 $\Delta$ arlD mutant, we observed that the number of cells with ArlD polar foci was ~20%

at an OD<sub>600</sub> of 0.01 (Nussbaum et al., 2020). In the  $\Delta$ minD2 $\Delta$ minD4 mutant, the formation of polar foci decreased, being present in only ~7% of cells at an OD<sub>600</sub> of 0.01, and continuing to decrease with increasing OD<sub>600</sub>. Additionally, it was previously observed that all cells in the stationary phase form foci corresponding to the archaellum motor complex. We observed comparable results in the  $\Delta$ arlD and  $\Delta$ minD2 $\Delta$ arlD mutants, with all cells having foci upon reaching the stationary phase at OD<sub>600</sub> 0.6 (Figure 6b). However, in the  $\Delta$ minD2 $\Delta$ minD4 $\Delta$ arlD mutants, we observed a consistent reduction in foci formation even at high OD<sub>600</sub>, which was not observed in the individual mutants (Figure 6b). Which suggests a synergistic effect or partially redundant role of MinD2 and MinD4 in the archaellum polar assembly.

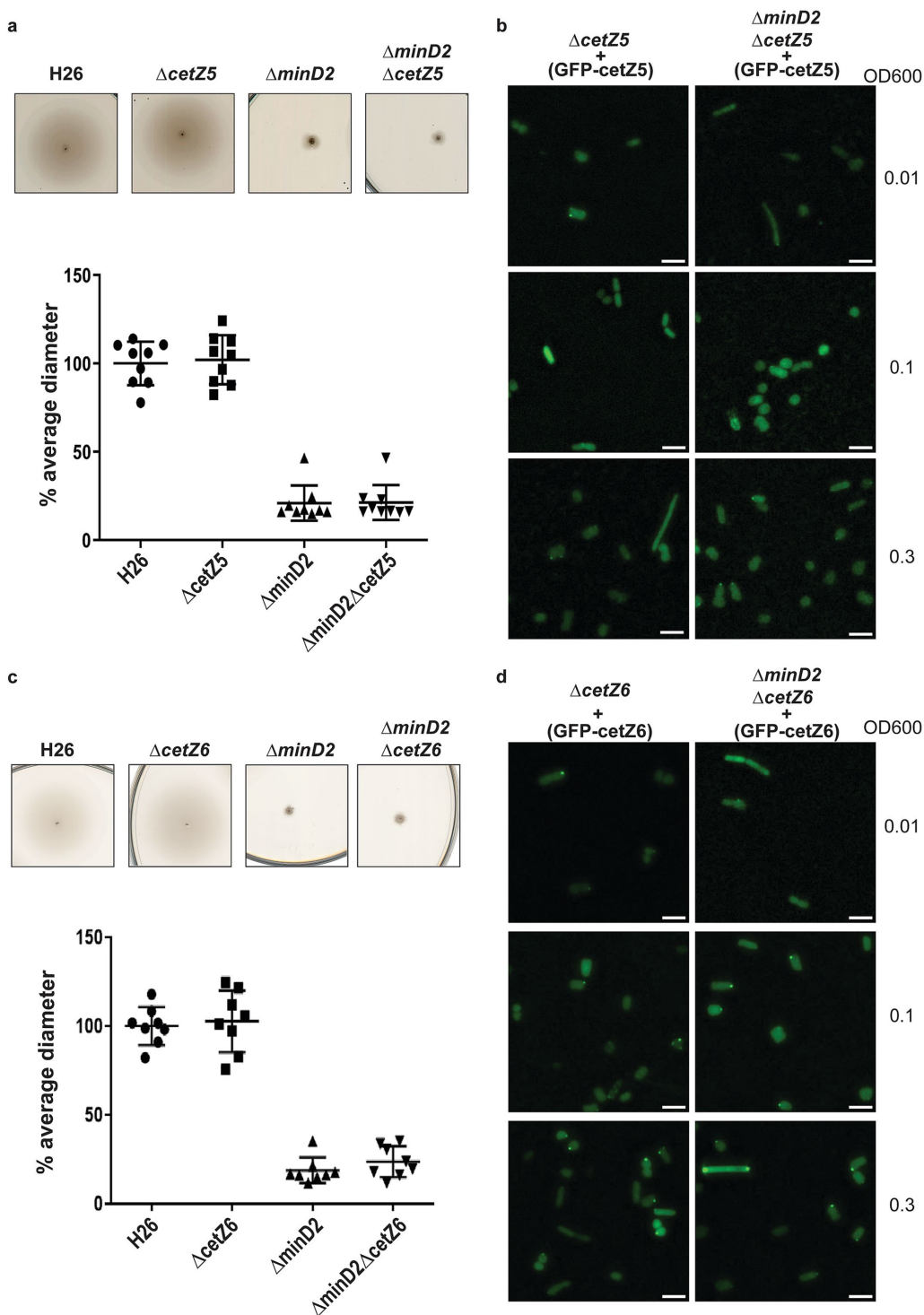
In *H. volcanii*, chemotaxis involves the assembly of chemosensory arrays, which are preferentially localized at the cell poles during the early log phase and become diffused as the cells enter stationary phase (Li et al., 2019). Therefore, we investigated whether MinD2 also influences the localization of chemosensory arrays, using the chemotaxis protein CheW as a marker for these clusters (Li et al., 2019). For this, we expressed GFP-CheW in cells lacking CheW ( $\Delta$ cheW) and cells lacking both CheW and MinD2 ( $\Delta$ minD2 $\Delta$ cheW). In  $\Delta$ cheW cells, expression of GFP-CheW led to polar foci in 78% of cells and diffused localization in 22% of cells (Li et al., 2019 and Figure 6c). By contrast, in  $\Delta$ minD2 $\Delta$ cheW cells, expression of GFP-CheW led to only 5% of the cells displaying polar chemosensory foci, while the remaining 95% of  $\Delta$ minD2 $\Delta$ cheW cells showed diffused GFP-CheW localization, suggesting the absence of chemosensory arrays localization (Figure 6c). Further analysis showed that the number of cells with CheW foci formation decreased substantially in  $\Delta$ cheW as the OD increased, while the localization of CheW reduces 5–0% in  $\Delta$ minD2 $\Delta$ cheW cells (Figure 6d).

Since previous studies have shown that MinD4 regulates the positioning of chemosensory arrays, we further investigated the links between MinD2 and MinD4 in modulating CheW localization. For this, we created the triple deletion mutant  $\Delta$ minD2 $\Delta$ minD4 $\Delta$ cheW, which has then been used to study the localization of GFP-CheW. Our results showed a further reduction in CheW foci formation in  $\Delta$ minD2 $\Delta$ minD4 $\Delta$ cheW cells compared to  $\Delta$ minD2 $\Delta$ cheW cells, with only 2% of cells showing polar GFP-CheW foci at OD<sub>600</sub> of 0.01. In the transition of OD<sub>600</sub> from 0.01 to 0.03, we observed GFP-CheW foci formation to be completely absent, with no cells displaying CheW foci (Figure 6d).

Collectively, these data show that MinD2 impacts the localization of both the motility and chemosensory machineries, in addition to the effect that MinD4 has on the localization of these cellular components.

## RNA-seq analysis reveals limited transcriptional changes in archaellum and chemotaxis gene upon minD2 deletion

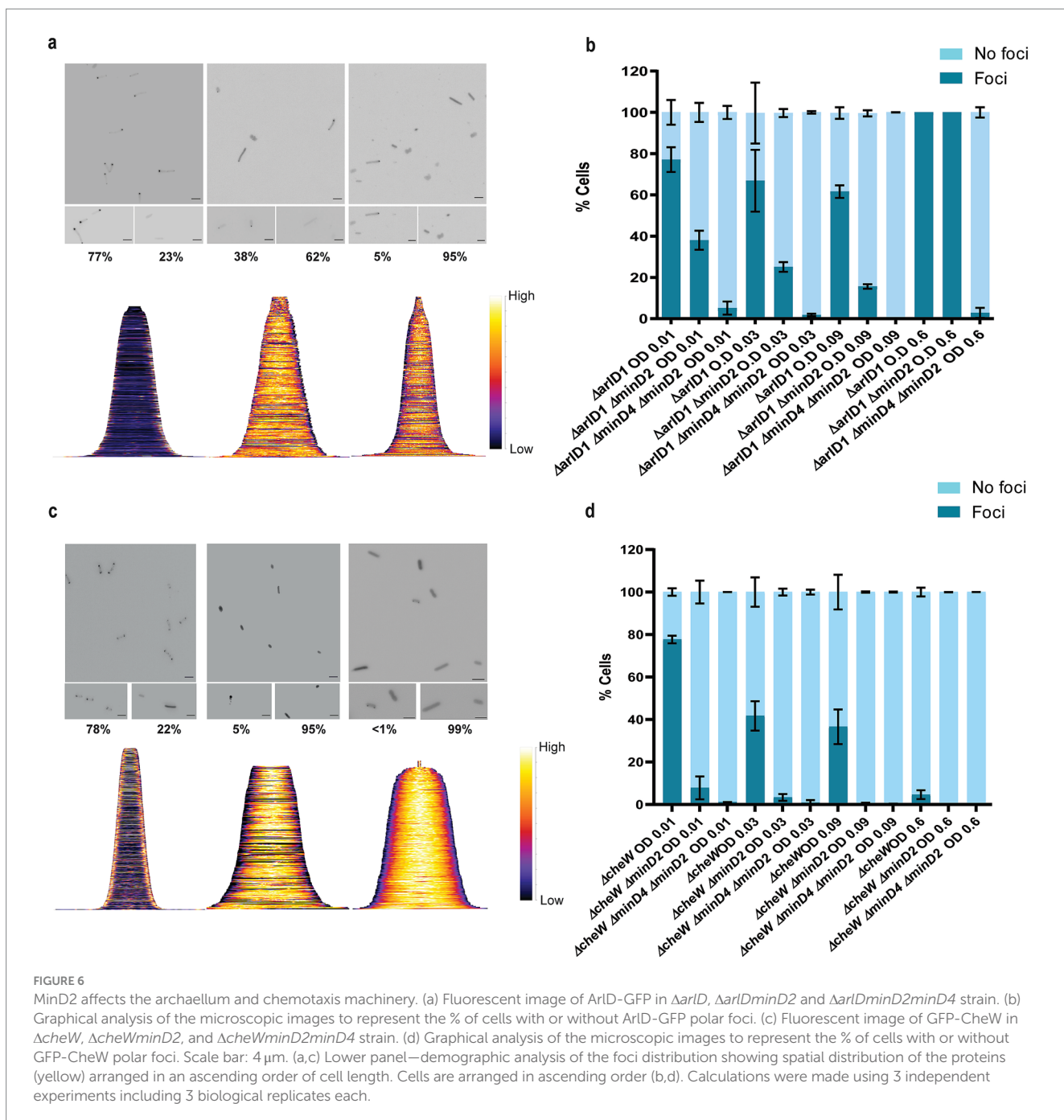
Given the pronounced effects of minD2 deletion on cell shape and motility, we explored whether these phenotypic changes can be explained by transcriptional alterations in the relevant genes. Therefore, RNA-seq analysis was performed on WT and  $\Delta$ minD2 strains at early-log (OD<sub>600</sub>: 0.02), mid-log (OD<sub>600</sub>: 0.3) and stationary phase (OD<sub>600</sub>: 2) to identify any differentially expressed genes (log<sub>2</sub>-fold changes: Supplementary Table 6, transcript per million values:

**FIGURE 5**

CetZ5 and CetZ6 do not have a motility phenotype and display diffused fluorescence. (a) Semi-solid agar-based motility assay for H26,  $\Delta\text{CetZ5}$  and double mutant,  $\Delta\text{minD2CetZ5}$ . (b) Localization of GFP-CetZ5 in  $\Delta\text{CetZ5}$  and  $\Delta\text{minD2CetZ5}$ . (c) Semi-solid agar-based motility assay for H26,  $\Delta\text{CetZ6}$  and double mutant,  $\Delta\text{minD2CetZ6}$ . (d) Localization of GFP-CetZ6 in  $\Delta\text{CetZ6}$  and  $\Delta\text{minD2CetZ6}$ . Scale bar: 4  $\mu\text{m}$ . Calculations were made using 3 independent experiments including 3 biological replicates each.

Supplementary Table 7). Despite the clear morphological and motility defects, no significant transcriptional changes in the core genes related to archaeum assembly or chemotaxis were consistent over all three growth stages (Figure 7a). Instead, some of the genes showed stage-dependent differences, including downregulation of

CetZ2 ( $\log_2$ -fold change: -2.3) and upregulation of PssA ( $\log_2$ -fold change: 1.1) during early growth phase, and upregulation of CheW ( $\log_2$ -fold change: 0.9) during stationary phase. In general, many significant transcriptional changes were observed in the early (down: 21.9%; up: 20.9%) and stationary phase (down: 12.1%; up: 19.8%),



but not at mid-exponential (down: 0.4%; up: 0.4%) (Figure 7b). From the 33 differentially regulated genes at OD<sub>600</sub> of 0.2 (mid), the loss of polar localization of the motility machinery could not be explained (Figure 7c). To detect any general trends, a functional enrichment analysis using clusters of orthologous groups was performed (Figure 7d and Supplementary Table 8). This analysis revealed the absence of consistently regulated and functionally related genes upon *minD2* deletion. Instead, a counter-regulation of metabolism groups C (energy production and conversion), G (carbohydrate transport and metabolism), E (amino acid transport and metabolism), and I (lipid transport and metabolism) could be observed, with genes that are downregulated during early growth phase but are later upregulated.

Together, these RNA-seq findings complement the previous localization studies and suggest that MinD2 regulates these processes at the level of protein localization rather than gene expression. This underscores the importance of MinD2 in maintaining cell morphology and motility through mechanisms beyond transcriptional control.

## Discussion

*Haloferax volcanii* encodes four homologs of the MinD protein, which unlike their counterparts in bacterial cells, are not involved in cell division and do not regulate the localization of the divisome (Nußbaum et al., 2020). Previous studies have started to elucidate the

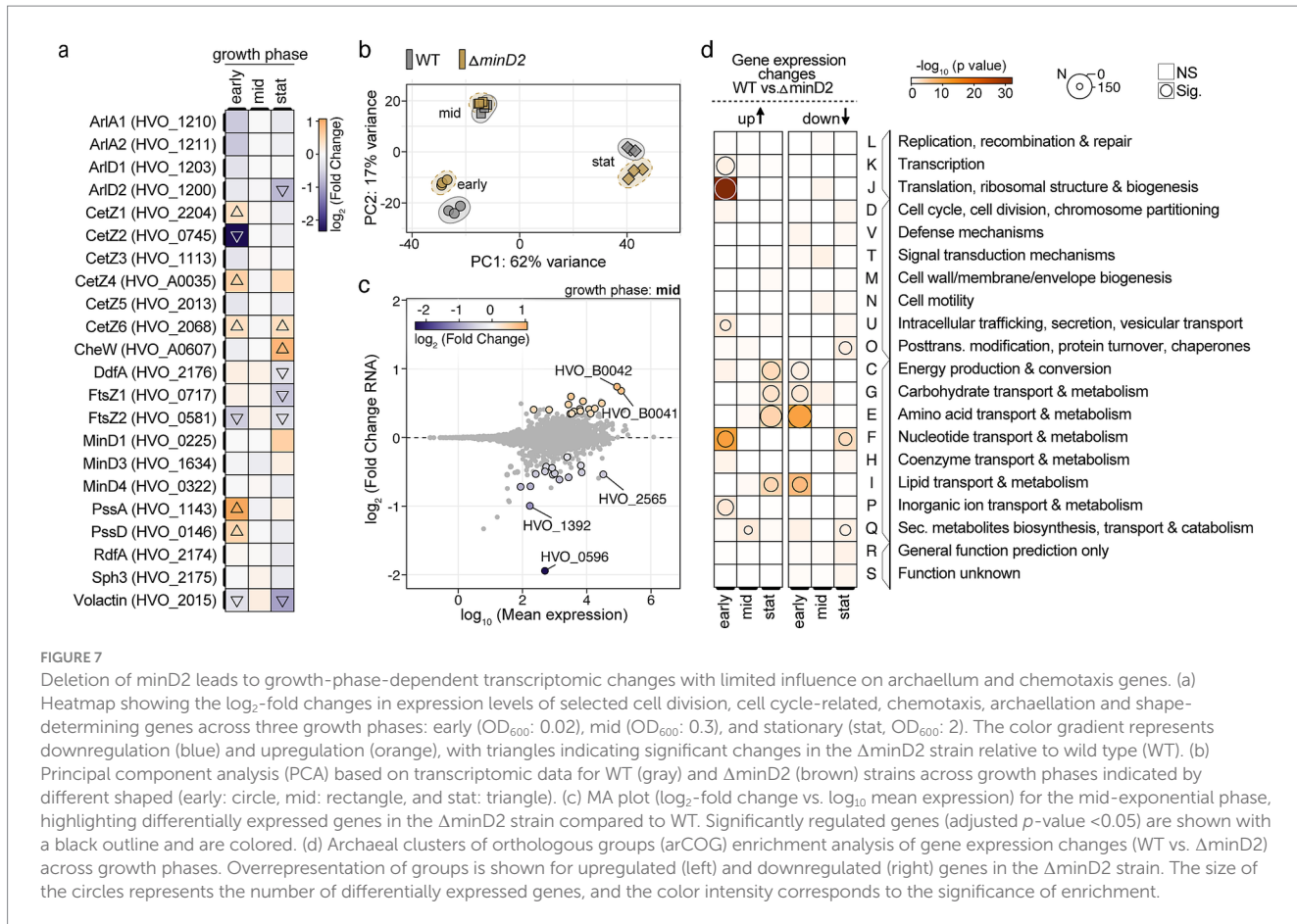


FIGURE 7

Deletion of minD2 leads to growth-phase-dependent transcriptomic changes with limited influence on archaeallum and chemotaxis genes. (a) Heatmap showing the log<sub>2</sub>-fold changes in expression levels of selected cell division, cell cycle-related, chemotaxis, archaeallation and shape-determining genes across three growth phases: early ( $OD_{600}$ : 0.02), mid ( $OD_{600}$ : 0.3), and stationary (stat,  $OD_{600}$ : 2). The color gradient represents downregulation (blue) and upregulation (orange), with triangles indicating significant changes in the ΔminD2 strain relative to wild type (WT). (b) Principal component analysis (PCA) based on transcriptomic data for WT (gray) and ΔminD2 (brown) strains across growth phases indicated by different shaped (early: circle, mid: rectangle, and stat: triangle). (c) MA plot ( $\log_2$ -fold change vs.  $\log_{10}$  mean expression) for the mid-exponential phase, highlighting differentially expressed genes in the ΔminD2 strain compared to WT. Significantly regulated genes (adjusted  $p$ -value <0.05) are shown with a black outline and are colored. (d) Archaeal clusters of orthologous groups (arCOG) enrichment analysis of gene expression changes (WT vs. ΔminD2) across growth phases. Overrepresentation of groups is shown for upregulated (left) and downregulated (right) genes in the ΔminD2 strain. The size of the circles represents the number of differentially expressed genes, and the color intensity corresponds to the significance of enrichment.

functions of MinD proteins in *H. volcanii*, particularly MinD4 (HVO\_0322), which governs the precise positioning of both the archaeallum and chemotaxis machineries, which are indispensable for enabling directional and purposeful motility (Nußbaum et al., 2020) in rod cells. Here, we further extend the characterization of the functions of MinD proteins in *H. volcanii* cells, focusing on MinD2. Our analyses underscored MinD2 as a regulatory protein in cell shape morphology (Figure 1) and motility (Figure 2), by enabling cells to retain a rod shape, particularly in the early growth phase. Furthermore, we demonstrate that MinD2 shows diffuse localization across the cell (Supplementary Figure 3) and likely interacts with a variety of partner proteins to mediate its effects (Figures 4, 5). By analyzing the localization of a variety of proteins involved in the formation of the archaeallum and chemotaxis complexes, we also reveal that MinD2 modulates the placement of the motility and chemotaxis machineries (Figure 6). Interestingly, RNA-seq analysis indicated no transcriptional changes in genes related to morphology or motility, despite the phenotype observed (Figure 7). Finally, we investigate the links between MinD2 and MinD4, showing that the two MinD homologues have synergistic roles in linking cell shape and motility in *H. volcanii* (Figure 6).

Studies on *H. volcanii* provide insights into the regulation of cell shape in response to environmental cues. The cells undergo remarkable transformations in cell shape during different growth phases and conditions. These changes, from rod-shaped to flat, polygonal pleomorphic disks (plate shaped), have been a subject of interest due to their potential roles in adaptation and survival

strategies (Halim et al., 2017; Li et al., 2019; de Silva et al., 2021). However, our understanding of the molecular mechanisms controlling archaeal cell shape determination is still developing. Previous studies identified proteins such as CetZ1, LonB, ArtA, PssA, and PssD as important regulators of this process (Duggin et al., 2015; Halim et al., 2017; Ferrari et al., 2020; Brown and Duggin, 2023). More recently, cell-shape mutants lacking the ability to form plates have been studied, including DdfA (disk determining factor), which is likely involved in the signaling pathways that determine cell shape. Additionally, studies on RdfA (rod-determining factor) and Sph3 (SMC-like protein) indicate that these proteins are also involved in the signal cascade that potentially regulates cell shape (Schiller et al., 2024). However, how these and other cell-shape determinants interact with each other, and how their activity is regulated by environmental conditions, remains unclear.

Our findings identify MinD2 as another protein that regulates cell shape in *H. volcanii* cells (Figure 1 and Supplementary Figure 2). One of the most distinctive features of the ΔminD2 mutant is its preponderance to form plate-shaped cells, including in the early log phase, highlighting the importance of MinD2 in maintaining the rod-shaped morphology characteristic of *H. volcanii* cells. Furthermore, while the presence of a plasmid delayed the rod-to-plate cell shape transition, particularly in early log phase, the majority of ΔminD2 + pTA1392 cells still displayed plate shape as the optical density of the cultures increased (Figure 1b). Therefore, although the presence of plasmid can partially prevent the loss of rod shape in the

$\Delta minD2$  mutant early on, the absence of MinD seems to dominate the phenotype, resulting in the majority of cells being plates.

While our findings demonstrate that MinD2 regulates cell shape, the mechanism by which MinD2 operates remains unclear. Notably, we find that MinD2 shows a diffuse localization pattern across the cell, rather than localizing to specific foci, such as the cell pole (Figure 3). Furthermore, our experiments with various variants of MinD2 suggest that its N-terminus is important for activity, potentially through interactions with protein partners (Figure 3). Indeed, we identified several potential interacting partners of MinD2, including HVO\_0596, CetZ5, and CetZ6. However, mutants lacking HVO\_0596, a protein transcribed from the same operon as MinD2, or either of the CetZs, showed no discernible phenotypes with regards to morphology (Figures 4, 5). Furthermore, our experiments with single vs. double mutants show that the observed impacts of motility in these mutants is primarily attributable to MinD2 (Figures 4, 5).

While future studies are needed to further elucidate how MinD2 regulates morphology and motility in *H. volcanii*, our findings provide some insights into the links between these two cellular processes. For example, we found that discoid  $\Delta minD2$  cells have a significant decrease in the number of archaella, which results in decreased motility (Figure 2). In addition, MinD2 deletion also impacted the positioning of the chemotaxis machinery (Figure 6). One possibility is that these changes in the localization of archaella and chemosensory arrays result from the observed changes in morphology in  $\Delta minD2$  cells, particularly their inability to retain rod shape. This possibility is supported by studies in other microbial species linking cell shape and the special organization of motility machinery. For example, in *E. coli*, chemosensory arrays preferably localize to the curved membrane (Strahl et al., 2015; Draper and Liphardt, 2017). Functional enrichment analysis further supported the notion that MinD2's effects are not driven by consistent changes in gene expression (Figure 7), indicating that MinD2 participates in the spatial organization of the archaeal cell pole. For example, some proteins, like bacterial ParA/MinD homologs (such as FlhG and ParC) rely on polar landmark proteins for localization (Lutkenhaus, 2012). In *H. volcanii*, the MinD4 homolog oscillates along the cell axis and is hypothesized to function similarly to polar landmark proteins, thereby influencing the proper positioning of both archaella and chemosensory arrays (Nußbaum et al., 2020). Notably, here we show that  $\Delta minD2\Delta minD4$  mutants have stronger defects in the positioning of the motility and chemosensory machinery (Figure 6) than  $\Delta minD4$  single mutants (Nußbaum et al., 2020; Figure 6), suggesting that MinD2 and MinD4 have non-redundant roles in these processes.

Based on our findings and previous studies, we propose a model for how MinD2 controls cell shape and motility in *H. volcanii* (Figure 8). In this model, while MinD4 is important for promoting the adequate positioning of polar proteins, some of these proteins can still find the 'probable' pole even in the absence of MinD4. This is in agreement with previous studies, which showed that while a reduced frequency of  $\Delta minD4$  mutant cells express archaella (20%) and chemosensory array (40%), some cells can still assemble these structures (Nußbaum et al., 2020). In the case of  $\Delta minD2$  mutants, we postulate that the loss of rod shape resulting from MinD2 absence influences the positioning of these machineries in most cells, although some can still assemble archaella and chemosensory arrays guided by polar cap proteins. In the absence of both MinD2 and MinD4, cells are always plate

shaped and polar MinD4 patches are not established. This combination may render proteins targeted to the poles unable to detect 'probable' poles and/or impair their interaction with different polar cap proteins. Under this scenario, the lack of both MinD2 and MinD4 leads to a synergistic effect, resulting in an almost complete absence of cells with archaellum (5%) or chemosensory (1%) machineries.

Morphological integrity and the determination of cell shape are pivotal aspects of microbial physiology. While these mechanisms are fairly well understood in bacteria, less is known about their archaeal counterparts. This study further advances our understanding of cell morphology determination in archaea by highlighting the pivotal role of the archaeal MinD2 homologue in modulating *H. volcanii* morphology. Notably, while bacterial Min proteins predominantly influence cell division, our observations suggest that MinD2 in archaea may have evolved or diversified to have more influence on cell morphology. Additionally, our findings support a model in which MinD2 contributes to cells retaining a rod-shape morphology, which enables polar cap proteins to recognize the cell poles, thereby supporting the assembly and adequate positioning of the motility and chemotaxis machinery. Furthermore, our findings add support to previous studies on MinD4 suggesting that archaeal MinD homologues have non-redundant roles in influencing cell shape and the positioning of motility and chemotaxis machinery. These findings contribute to a deeper understanding of the intricate regulatory network governing cellular processes in archaea, and set the stage for future studies aimed at uncovering the detailed molecular mechanisms by which MinD proteins modulate haloarchaeal physiology.

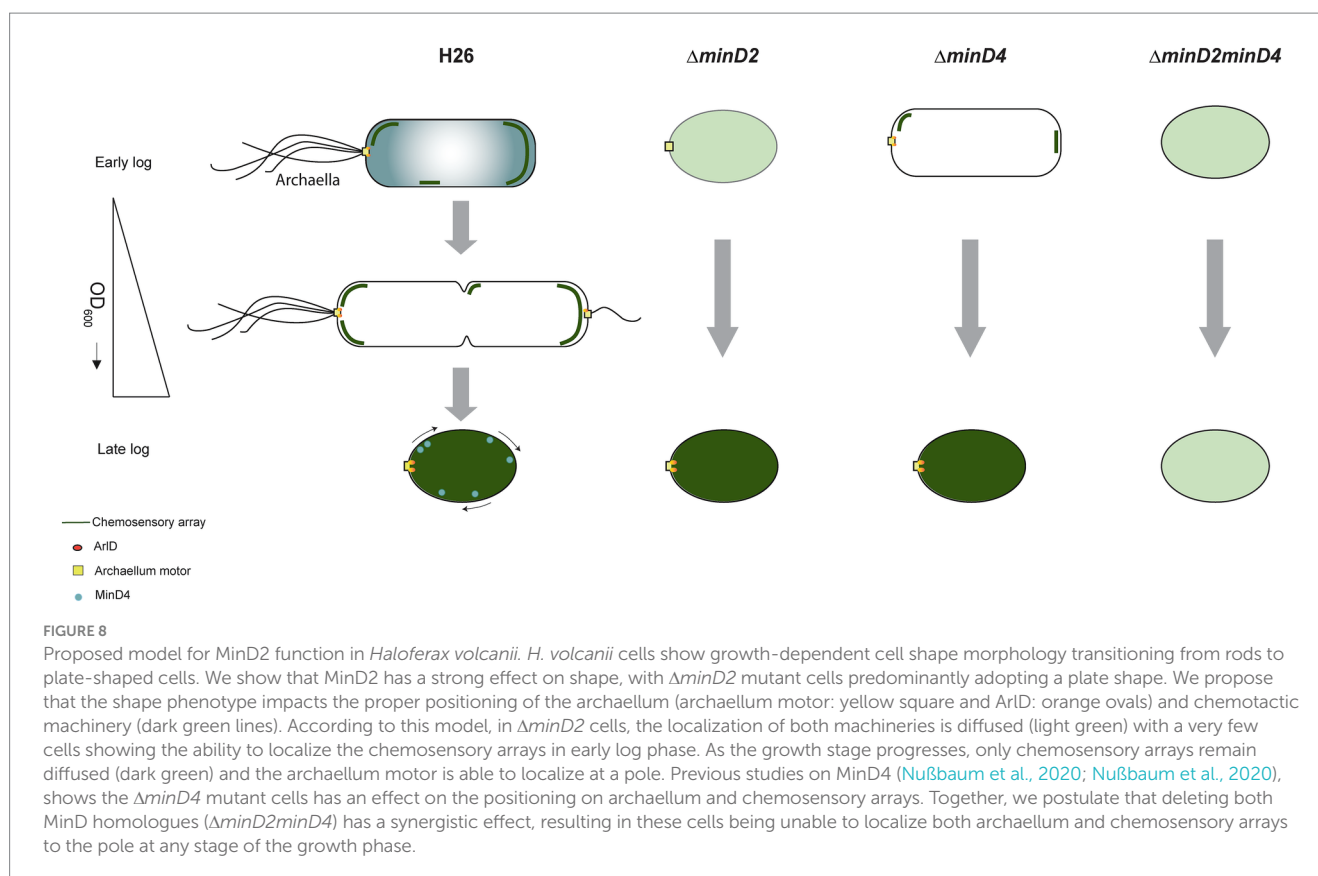
## Materials and methods

All chemicals have been purchased from Roth or Sigma unless stated otherwise.

## Strain and growth condition

*Escherichia coli* strains were cultured in LB (Luria Broth)-medium or grown on LB agar plates, with the necessary antibiotics (100 µg/mL ampicillin, 30 µg/mL chloramphenicol, 25 µg/mL kanamycin) and grown at 37°C. Liquid cultures were constantly shaken at 150 rpm.

*Haloferax volcanii* H26 cells were grown in YPC medium [0.5% (w/v) yeast extract (Difco), 0.1% (w/v) peptone (Oxoid), and 0.1% (w/v) casamino acids (Difco)] dissolved in 18% buffered Salt Water (SW) (144 g/L NaCl, 18 g/L MgCl<sub>2</sub> \* 6 H<sub>2</sub>O, 21 g/L MgSO<sub>4</sub> \* 7 H<sub>2</sub>O, 4.2 g/L KCl, 12 mM Tris/HCl, pH 7.5), supplemented with 3 mM CaCl<sub>2</sub>, adjusted to a pH of 7.2 with KOH for transformations. For experiments, CAB medium was used [i.e. CA medium (0.5% (w/v) casamino acid) dissolved in 18% SW, supplemented with 3 mM CaCl<sub>2</sub>, and 0.8 µg/mL of thiamine, and 0.1 µg/mL of biotin, adjusted to a pH of 7.2 with KOH and supplemented with trace elements solutions (Duggin et al., 2015)] was used. For each experiment, a single colony was inoculated into 5 mL medium and diluted to a larger volume on the subsequent day. This dilution was crucial to ensure an appropriate cell density for subsequent experiments. By adjusting the OD<sub>600</sub> to the desired value, it was possible to obtain a consistent starting point on the day of the experiment.



For strains with an auxotrophic mutation grown in CA/CAB medium, the medium was supplemented with 50 µg/mL uracil for *DpyrE2*. Alternatively, the strains were transformed with a plasmid carrying the respective gene for viable growth. For growth curve, cells were grown in 15 mL culture volume and measured with cell growth quantifier (CGQ) (Aquila biolabs GmbH) at 45°C and shaking at 120 rpm.

## Genetic modification of *Haloferax volcanii*

Transformation in H26 based on uracil selection via the Polyethylene glycol 600 (PEG600) along with gene deletion and expression studies were conducted as described previously (Allers et al., 2004). For transformation into *H. volcanii*, non-methylated plasmids were extracted from *E. coli* *dam*<sup>-</sup>/*dcm*<sup>-</sup> (C2925I, NEB). Mutant strains generated and used are described in Supplementary Table 1. Plasmids created for knockout mutants are described in Supplementary Table 2. Primers to create knockout plasmids were based on pTA131, are described in Supplementary Table 3.

## Growth curve

Glycerol stocks were streaked on solid agar medium substituted with uracil and incubated at 45°C for 5 days. A single colony from plates was used to inoculate 5 mL of media on day 1. Strains without plasmid were grown in CAB with 50 µg/mL uracil and strains with plasmid pTA1392 (containing *pfdx-pyrE2*) were grown in CAB medium without supplements. To generate a growth curve, the

obtained culture was inoculated on day 2 at a starting OD<sub>600</sub> of 0.05. The cell density was measured with cell growth quantifier (CGQ) (Aquila biolabs GmbH) at 45°C and shaking at 120 rpm and measurement were taken every 300 s.

## Spot survival assay

To assess the growth and viability of the H26 and  $\Delta\text{minD2}$  (transformed with pTA1392) strains, cells were cultured in 5 mL CAB medium at 45°C to an OD<sub>600</sub> of 0.2. On the next day, cell cultures were set to a theoretical OD<sub>600</sub> of 0.2. A serial dilution was prepared until a dilution of 10<sup>5</sup> and 5 µL of each dilution per strain was spotted on CA-plates. The plates were incubated for 2 days at 45°C in sealed plastic bags.

## Microscopy

The cell shape was analyzed by imaging the cells with an inverted phase contrast light microscope (Zeiss Axio Observer Z.1). The cells were grown in 5 mL of the respective medium and diluted in 20 mL media volume the next day in order to achieve an OD<sub>600</sub> of 0.01 the day after. For each culture, 5 µL sample was collected from different growth phases and dropped at the center of an agarose pad (0.3% (w/v) agarose dissolved in 18% SW). On drying, the pad was covered with a cover slip and imaged. The images were acquired at 100x magnification using the oil immersion phase contrast (PH3) channel. All sampled were analyzed in triplicated. Fluorescence microscopy images were acquired on Zeiss Axio Observer Z.1 (ex: 450–490 nm

em: 500–550 nm filter from Chroma®), equipped with a heated XL-52000 Incubator running VisiVIEW® software for MinD4 and CheW.

## Image analysis

The phase contrast images from the microscopy were analyzed using Fiji (Schindelin et al., 2012) combined with MicrobeJ plugin (Ducret et al., 2016). For the analysis, cells that formed aggregates or were fragmented were discarded from the calculation. The circularity of the cells was automatically calculated. The diameter of each analyzed cell was thereon calculated and grouped into 6 bins in the range interval of 0.1 to 1. The parameters used for circularity were as previously defined in Patro et al. (2023).

## Transmission electron microscopy

Cells were harvested at 2000 g for 15 min. The resulting pellet was resuspended to a theoretical O.D of 10. Five µL of cells of the cell suspension was applied to a glow discharged carbon coated copper grid (Plano GmbH, Wetzlar Germany) and incubated for 10 s. The excess liquid was blotted away. The cells were then stained with 2% uranyl acetate (w/v). Cells were imaged using Zeiss Leo 912 Omega (tungsten) operated at 80 kV and images were taken using Dual speed 2K on Axis charge-coupled device (COD) camera (TRS, Sharp-Eye).

## Motility assay

Semi-solid agar plates were prepared using 0.33% agar in CA medium supplemented with 1 mM tryptophan. Cultures grown at OD<sub>600</sub> 0.3 were inoculated into the plates using stab techniques, and the plates were then incubated at 45°C for 4 days. To compare the motility of different strains, all strains were spotted on the same plate. For each strain, a minimum of 3 technical replicates and 3 biological replicates were conducted. After 4 days, the diameter of the motility ring was assessed.

## RNA sequencing for differential gene expression analysis

### RNA extraction

RNA was extracted from the *minD2* deletion strain during lag phase (OD<sub>600</sub> 0.02), exponential phase (OD<sub>600</sub> 0.3), and stationary phase (OD<sub>600</sub> 2), and WT H26 was used as control. Cultures were scaled to 1 L for lag phase, 20 mL for exponential phase, and 3 mL for stationary phase, with 5 replicates per strain and growth phase. Once the cells reached the desired optical density, they were harvested and resuspended to a theoretical OD<sub>600</sub> of 5. Approx. 2 mL of the resuspended cells were transferred to a new tube and centrifuged. RNA was isolated using the RNeasy® Plus Mini Kit from QIAGEN. The cell pellets were resuspended in 600 µL of RLT-plus buffer, and RNA extraction was performed according to the Qit. The RNA was then eluted in 31 µL of RNase-free water (Roth®), rapidly frozen in liquid nitrogen, and stored at -80°C.

## Library preparation and sequencing

RNA quality was assessed using a Bioanalyzer, with only samples exhibiting RNA integrity number (RIN) values of 8.5 or higher being used. Prior to library preparation, RNA samples underwent Turbo DNase treatment according to the manufacturer's instructions (Ambion, 1 unit) to remove any residual DNA. For each experimental condition, four independent biological replicates were prepared. To ensure the removal of ribosomal RNA, 2 µg of input RNA was treated with a Ribopool designed specifically for *Haloflexax volcanii* (siTOOLs) according to the manufacturer's instructions.

Library preparation and RNA-sequencing were carried out as described in the Illumina "Stranded mRNA Prep Ligation" Reference Guide, the Illumina NextSeq 2000 Sequencing System Guide (Illumina, Inc., San Diego, CA, USA), and the KAPA Library Quantification Kit - Illumina/ABI Prism (Roche Sequencing Solutions, Inc., Pleasanton, CA, USA).

In brief, omitting the initial mRNA purification step with oligo(dT) magnetic beads, approximately 5 ng of rRNA depleted archaeal RNA was fragmented to an average insert size of 200–400 bases using divalent cations under elevated temperature (94°C for 8 min). Next, the cleaved RNA fragments were reverse transcribed into first strand complementary DNA (cDNA) using reverse transcriptase and random hexamer primers. Thereby Actinomycin D was added to allow RNA-dependent synthesis and to improve strand specificity by preventing spurious DNA-dependent synthesis. Blunt-ended second strand cDNA was synthesized using DNA Polymerase I, RNase H and dUTP nucleotides. The incorporation of dUTP, in place of dTTP, quenches the second strand during the later PCR amplification, because the polymerase does not incorporate past this nucleotide. The resulting cDNA fragments were adenylated at the 3' ends and the pre-index anchors were ligated. Finally, DNA libraries were created using a 15 cycles PCR to selectively amplify the anchor-ligated DNA fragments and to add the unique dual indexing (i7 and i5) adapters. The bead purified libraries were quantified using the KAPA Library Quantification Kit. Equimolar amounts of each library were sequenced on an Illumina NextSeq 2000 instrument controlled by the NextSeq 2000 Control Software (NCS) v1.5.0.42699, using one 50 cycles P3 Flow Cell with the dual index, single-read (SR) run parameters. Image analysis and base calling were done by the Real Time Analysis Software (RTA) v3.10.30. The resulting .cbcl files were converted into .fastq files with the bcl2fastq v2.20 software. Library preparation and RNA-sequencing were performed at the Genomics Core Facility "KFB-Center of Excellence for Fluorescent Bioanalytics" (University of Regensburg, Regensburg, Germany<sup>1</sup>).

### Differential gene expression analysis

Raw sequencing reads in FASTQ format were initially processed for quality control and trimming using fastp (v. 0.23.2) (Chen et al., 2018). This step removed low-quality bases and adapter sequences with parameters set to `--cut\_front --cut\_tail\_q 30` to ensure high-quality data. The filtered reads were then aligned to the *Haloflexax volcanii* DS2 reference genome using Bowtie2 (v. 2.5.0) with default settings (Langmead and Salzberg, 2012). The resulting sequence alignment files in SAM format were converted to BAM using samtools (v. 1.17) for efficient

<sup>1</sup> [www.kfb-regensburg.de](http://www.kfb-regensburg.de)

handling and analysis (Li et al., 2009). To identify differentially expressed genes, we followed the guidelines provided in the Bioconductor vignette for the DESeq2 package (v. 1.42.1) (Love et al., 2014). Gene counts were derived from RNA-seq data using featureCounts (part of RSubread package v. 2.16.1) with a custom GTF file (Liao et al., 2019). This file was created by filtering the *H. volcanii* DS2 GFF annotation file, obtained from the NCBI, to include only features with the type 'gene' or 'gene.'. Principal component analysis (PCA) was performed on variance-stabilizing transformed data to assess overall data structure and identify outliers. Specifically, outlier replicates were removed based on visual inspection, including wild type early phase replicate 4, wild type mid phase replicate 1, wild type stationary phase replicate 1,  $\Delta minD2$  early phase replicate 4 and  $\Delta minD2$  stationary phase replicate 1. Differential expression analysis was conducted by comparing the wild type and  $\Delta minD2$  strains across different growth conditions to identify growth-dependent changes in gene expression.

## Functional enrichment analysis based on arCOG classification

To elucidate the functional characteristics of differentially expressed genes, we performed a functional enrichment analysis using the Archaeal Clusters of Orthologous Genes (arCOG) classification, as described previously (Makarova et al., 2015; Grünberger et al., 2023). Briefly, arCOGs for *H. volcanii* were retrieved from Makarova et al. (2015) and gene set enrichment analysis performed with the goseq package (v. 1.54.0) in R (Young et al., 2010). For each growth condition, a background file was generated from all genes that could be detected. Next, *p*-values for overrepresentation of arCOG terms in the differentially expressed genes were calculated separately for up-and downregulated genes based on RNA-seq data. Significance was determined using a threshold of 0.05 to identify terms that were significantly enriched.

## Structural analyses

The AlphaFold models for MinD2 and HVO\_0596 were generated with AlphaFold 3 Google colab (Abramson et al., 2024) and further analyzed by ChimeraX (Meng et al., 2023).

## Data availability statement

The original contributions presented in the study are included in the article/[Supplementary material](#), further inquiries can be directed to the corresponding author. RNA sequencing data are available at the European Nucleotide Archive (ENA, <https://www.ebi.ac.uk/ena>) under project accession number PRJEB79934.

## Author contributions

MP: Conceptualization, Data curation, Formal analysis, Investigation, Methodology, Software, Validation, Visualization, Writing – original draft, Writing – review & editing. FG: Formal analysis, Investigation, Visualization, Writing – review & editing. SS: Formal analysis, Investigation, Writing – review & editing. SG: Formal analysis, Investigation, Writing – review & editing. MR-F: Formal analysis, Investigation, Writing – review & editing. PN: Formal analysis, Investigation, Writing – review & editing. DG: Supervision,

Resources, Writing – review & editing. SI: Conceptualization, Formal analysis, Investigation, Supervision, Writing – review & editing. S-VA: Conceptualization, Funding acquisition, Methodology, Project administration, Resources, Supervision, Validation, Writing – original draft, Writing – review & editing.

## Funding

The author(s) declare that financial support was received for the research, authorship, and/or publication of this article. MP was supported by the German Research Foundation on grant number AL1206/4-3. SG was supported by the German Science Foundation (DFG) project number 505545313 (AL1206/14-1) to S-VA. PN and SI were supported by the VW Foundation by a Momentum grant to S-VA (AZ 94993). SS was supported by the German Research Foundation under project number 403222702-SFB 1381 to S-VA. The TEM (Hitachi HT7800) was funded by the DFG project number 42689454 and is operated by the faculty of biology at the University of Freiburg as a partner unit within the Microscopy and Image Analysis Platform (MIAP) and Life Imaging Centre (LIC), Freiburg.

## Acknowledgments

We thank Katharina Vogel for her technical assistance. Molecular graphics and analyses performed with UCSF ChimeraX, developed by the Resource for Biocomputing, Visualization, and Informatics at the University of California, San Francisco, with support from National Institutes of Health R01-GM129325 and the Office of Cyber Infrastructure and Computational Biology, National Institute of Allergy and Infectious Diseases. We acknowledge support by the Open Access Publication Fund of the University of Freiburg.

## Conflict of interest

The authors declare that the research was conducted in the absence of any commercial or financial relationships that could be construed as a potential conflict of interest.

The author(s) declared that they were an editorial board member of Frontiers, at the time of submission. This had no impact on the peer review process and the final decision.

## Publisher's note

All claims expressed in this article are solely those of the authors and do not necessarily represent those of their affiliated organizations, or those of the publisher, the editors and the reviewers. Any product that may be evaluated in this article, or claim that may be made by its manufacturer, is not guaranteed or endorsed by the publisher.

## Supplementary material

The Supplementary material for this article can be found online at: <https://www.frontiersin.org/articles/10.3389/fmicb.2024.1474570/full#supplementary-material>

## References

- Abramson, J., Adler, J., Dunger, J., Evans, R., Green, T., Pritzel, A., et al. (2024). Accurate structure prediction of biomolecular interactions with AlphaFold 3. *Nature* 630, 493–500. doi: 10.1038/s41586-024-07487-w
- Allers, T., Ngo, H. P., Mevarech, M., and Lloyd, R. G. (2004). Development of additional selectable markers for the halophilic archaeon *Haloferax volcanii* based on the leuB and trpA genes. *Appl. Environ. Microbiol.* 70, 943–953. doi: 10.1128/AEM.70.2.943-953.2004
- Atmakuri, K., Cascales, E., Burton, O. T., Banta, L. M., and Christie, P. J. (2007). Agrobacterium ParA/MinD-like VirC1 spatially coordinates early conjugative DNA transfer reactions. *EMBO J.* 26, 2540–2551. doi: 10.1038/sj.emboj.7601696
- Babski, J., Haas, K. A., Näther-Schindler, D., Pfeiffer, F., Förstner, K. U., Hammelmann, M., et al. (2016). Genome-wide identification of transcriptional start sites in the haloarchaeon *Haloferax volcanii* based on differential RNA-Seq (dRNA-Seq). *BMC Genomics* 17:629. doi: 10.1186/s12864-016-2920-y
- Baxter, J. C., and Funnell, B. E. (2014). Plasmid partition mechanisms. *Microbiol. Spectr.* 2. doi: 10.1128/microbiolspec.PLAS-0023-2014
- Brown, H. J., and Duggin, I. G. (2023). Diversity and potential multifunctionality of archaeal CetZ tubulin-like cytoskeletal proteins. *Biomol. Ther.* 13:34. doi: 10.3390/biom13010134
- Brown, H. J., Islam, M. I., Ruan, J., Baker, M. A. B., Ithurbide, S., and Duggin, V. O. R. C. I. D. P. I. G. (2024). CetZ-dependent assembly and positioning of the motility machinery in haloarchaea. *bioRxiv*. doi: 10.1101/2024.05.02.592137
- Chen, S., Zhou, Y., Chen, Y., and Gu, J. (2018). Fastp: an ultra-fast all-in-one FASTQ preprocessor, in. *Bioinformatics* 34, i884–i890. doi: 10.1093/bioinformatics/bty560
- de Silva, R. T., Abdul-Halim, M. F., Pittrich, D. A., Brown, H. J., Pohlschroder, M., and Duggin, I. G. (2021). Improved growth and morphological plasticity of *Haloferax volcanii*. *Microbiology* 167:001012. doi: 10.1099/MIC.0.001012
- Draper, W., and Liphardt, J. (2017). Origins of chemoreceptor curvature sorting in *Escherichia coli*. *Nat. Commun.* 8:14838. doi: 10.1038/ncomms14838
- Ducret, A., Quardokus, E. M., and Brun, Y. V. (2016). MicrobeJ, a tool for high throughput bacterial cell detection and quantitative analysis. *Nat. Microbiol.* 1:16077. doi: 10.1038/NMICROBIOL.2016.77
- Duggin, I. G., Aylett, C. H. S., Walsh, J. C., Michie, K. A., Wang, Q., Turnbull, L., et al. (2015). CetZ tubulin-like proteins control archaeal cell shape. *Nature* 519, 362–365. doi: 10.1038/nature13983
- Esquivel, R. N., Schulze, S., Xu, R., Hippler, M., and Pohlschroder, M. (2016). Identification of *Haloferax volcanii* pilin N-glycans with diverse roles in pilus biosynthesis, adhesion, and microcolony formation. *J. Biol. Chem.* 291, 10602–10614. doi: 10.1074/jbc.M115.693556
- Ferrari, M. C., Cerletti, M., Paggi, R. A., Troetschel, C., Poetsch, A., and De Castro, R. E. (2020). The LonB protease modulates the degradation of CetZ1 involved in rod-shape determination in *Haloferax volcanii*. *J. Proteome* 211:103546. doi: 10.1016/j.jprot.2019.103546
- Grüninger, F., Schmid, G., Ahmad, Z. El, Fenk, M., Vogl, K., Reichelt, R., et al. (2023). *MBio*:14. doi: 10.1128/mbio.02174-23. Uncovering the temporal dynamics and regulatory networks of thermal stress response in a hyperthermophile using transcriptomics and proteomics, 14
- Halim, M. F. A., Stoltzfus, J. D., Schulze, S., Hippler, M., and Pohlschroder, M. (2017). ArtA-dependent processing of a tat substrate containing a conserved tripartite structure that is not localized at the C terminus. *J. Bacteriol.* 199:e00802-16. doi: 10.1128/JB.00802-16
- Hu, Z., and Lutkenhaus, J. (2003). A conserved sequence at the C-terminus of MinD is required for binding to the membrane and targeting MinC to the septum. *Mol. Microbiol.* 47, 345–355. doi: 10.1046/j.1365-2958.2003.03321.x
- Ithurbide, S., de Silva, R. T., Brown, H. J., Shinde, V., and Duggin, I. G. (2024). A vector system for single and tandem expression of cloned genes and multi-colour fluorescent tagging in *Haloferax volcanii*. *Microbiology* 170:170. doi: 10.1099/mic.0.001461
- Jalal, A. S. B., and Le, T. B. K. (2020). Bacterial chromosome segregation by the ParABS system. *Open Biol.* 10:200097. doi: 10.1098/rsob.200097
- Jeoung, J. H., Giese, T., Grünwald, M., and Dobbek, H. (2009). CooC1 from *Carboxydotothermus hydrogenoformans* is a nickel-binding ATPase. *Biochemistry* 48, 11505–11513. doi: 10.1021/bi901443z
- Langmead, B., and Salzberg, S. L. (2012). Fast gapped-read alignment with bowtie 2. *Nat. Methods* 9, 357–359. doi: 10.1038/nmeth.1923
- Leipe, D. D., Wolf, Y. I., Koonin, E. V., and Aravind, L. (2002). Classification and evolution of P-loop GTPases and related ATPases. *J. Mol. Biol.* 317, 41–72. doi: 10.1006/jmbi.2001.5378
- Li, H., Handsaker, B., Wysoker, A., Fennell, T., Ruan, J., Homer, N., et al. (2009). The sequence alignment/map format and SAMtools. *Bioinformatics* 25, 2078–2079. doi: 10.1093/bioinformatics/btp352
- Li, Z., Kinoshita, Y., Rodriguez-Franco, M., Nußbaum, P., Braun, F., Delpech, F., et al. (2019). Positioning of the motility machinery in halophilic archaea. *mBio* 10:e00377-19. doi: 10.1128/mBio.00377-19
- Liao, Y., Smyth, G. K., and Shi, W. (2019). The R package Rsubread is easier, faster, cheaper and better for alignment and quantification of RNA sequencing reads. *Nucleic Acids Res.* 47:e47. doi: 10.1093/nar/gkz114
- Love, M. I., Huber, W., and Anders, S. (2014). Moderated estimation of fold change and dispersion for RNA-seq data with DESeq2. *Genome Biol.* 15:550. doi: 10.1186/s13059-014-0550-8
- Lutkenhaus, J. (2007). Assembly dynamics of the bacterial minCDE system and spatial regulation of the z ring. *Annu. Rev. Biochem.* 76, 539–562. doi: 10.1146/annurev.biochem.75.103004.142652
- Lutkenhaus, J. (2012). The ParA/MinD family puts things in their place. *Trends Microbiol.* 20, 411–418. doi: 10.1016/j.tim.2012.05.002
- Makarova, K. S., Wolf, Y. I., and Koonin, E. V. (2015). Archaeal clusters of orthologous genes (arCOGs): an update and application for analysis of shared features between thermococcales, methanococcales, and methanobacterales. *Life* 5, 818–840. doi: 10.3390/life50101818
- Meng, E. C., Goddard, T. D., Pettersen, E. F., Couch, G. S., Pearson, Z. J., Morris, J. H., et al. (2023). UCSF ChimeraX: tools for structure building and analysis. *Protein Sci.* 32:e4792. doi: 10.1002/pro.4792
- Nußbaum, P., Ithurbide, S., Walsh, J. C., Patro, M., Delpech, F., Rodriguez-Franco, M., et al. (2020). An oscillating MinD protein determines the cellular positioning of the motility machinery in Archaea. *Curr. Biol.* 30, 4956–4972.e4. doi: 10.1016/j.cub.2020.09.073
- Patro, M., Duggin, I. G., Albers, S.-V., and Ithurbide, S. (2023). Influence of plasmids, selection markers and auxotrophic mutations on *Haloferax volcanii* cell shape plasticity. *Front. Microbiol.* 14:1270665. doi: 10.3389/fmicb.2023.1270665
- Pradhan, P., Taviti, A. C., and Beuria, T. K. (2024). The bacterial division protein MinDE has an independent function in flagellation. *J. Biol. Chem.* 300:107117. doi: 10.1016/j.jbc.2024.107117
- Pulianmackal, L. T., Limcaoco, J. M. I., Ravi, K., Yang, S., Zhang, J., Tran, M. K., et al. (2023). Multiple ParA/MinD ATPases coordinate the positioning of disparate cargos in a bacterial cell. *Nat. Commun.* 14:3255. doi: 10.1038/s41467-023-39019-x
- Ringgaard, S., Schirner, K., Davis, B. M., and Waldor, M. K. (2011). A family of ParA-like ATPases promotes cell pole maturation by facilitating polar localization of chemotaxis proteins. *Genes Dev.* 25, 1544–1555. doi: 10.1101/gad.2061811
- Schiller, H., Kouassi, J., Hong, Y., Rados, T., Kwak, J., DiLucido, A., et al. (2024). Identification and characterization of structural and regulatory cell-shape determinants in *Haloferax volcanii*. *Nat. Commun.* 15:1414. doi: 10.1038/s41467-024-45196-0
- Schindelin, J., Arganda-Carreras, I., Frise, E., Kaynig, V., Longair, M., Pietzsch, T., et al. (2012). Fiji: an open-source platform for biological-image analysis. *Nat. Methods* 9, 676–682. doi: 10.1038/nmeth.2019
- Strahl, H., Ronneau, S., González, B. S., Klutsch, D., Schaffner-Barbero, C., and Hamoen, L. W. (2015). Transmembrane protein sorting driven by membrane curvature. *Nat. Commun.* 6:8728. doi: 10.1038/ncomms9728
- Szklarczyk, D., Morris, J. H., Cook, H., Kuhn, M., Wyder, S., Simonovic, M., et al. (2017). The STRING database in 2017: quality-controlled protein-protein association networks, made broadly accessible. *Nucleic Acids Res.* 45, D362–D368. doi: 10.1093/nar/gkw937
- Young, M. D., Wakefield, M. J., Smyth, G. K., and Oshlack, A. (2010). Gene ontology analysis for RNA-seq: accounting for selection bias. *Genome Biol.* 11:R14. doi: 10.1186/gb-2010-11-2-r14